We are IntechOpen, the world's leading publisher of Open Access books Built by scientists, for scientists

4,800
Open access books available

122,000
International authors and editors

135M
Downloads

Our authors are among the

154
Countries delivered to

TOP 1%
most cited scientists

12.2%
Contributors from top 500 universities

CLARIVATE ANALYTICS BOOK CITATION INDEX INDEXED

WEB OF SCIENCE™

Selection of our books indexed in the Book Citation Index in Web of Science™ Core Collection (BKCI)

Interested in publishing with us?
Contact book.department@intechopen.com

Numbers displayed above are based on latest data collected.
For more information visit www.intechopen.com

6

Numerical Simulation of Converter Fed Squirrel Cage Induction Motors

C. Grabner
Electric Drive Technologies, Austrian Institute of Technology
Giefinggasse 2, 1210 Vienna, Austria

1. Introduction

Electrical drive systems applied for very simple industrial pump, fan or compressor applications require different torque/speed profiles in different operational states (Heintze et al., 1971). This is often realized by robust and reliable converter-fed squirrel cage induction motors as exemplarity depicted in Fig.1.

Fig. 1. Family of variable speed drive systems consisting of induction motors with according power converters

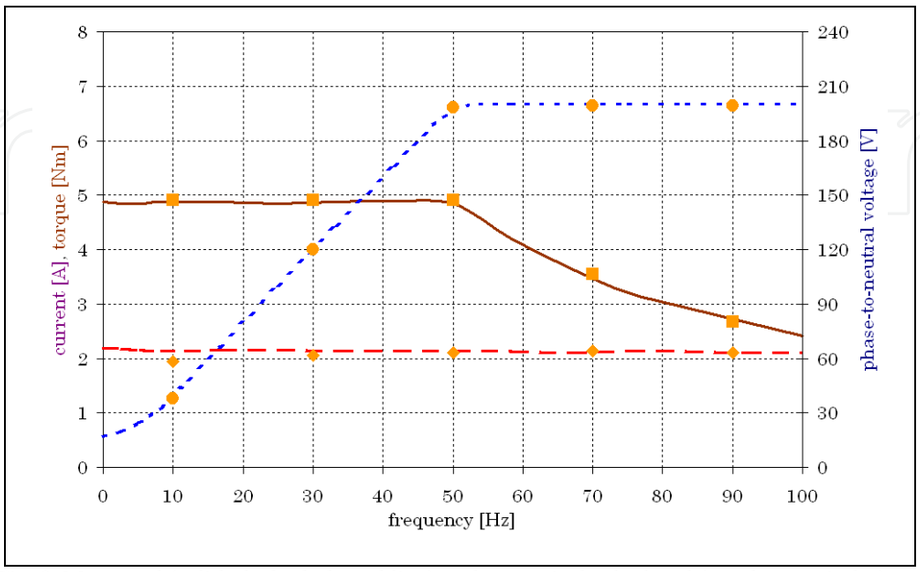

Fig. 2. Measured (solid, dashed, dotted line) and numerical calculated (quadrates, circles) effective voltage (blue), effective current (magenta) and mechanical torque (brown) versus the supply frequency for the steady-state S1-duty

The used V/f control technology needs thereby a voltage magnitude variation in dependency on the drive frequency as it is exemplarily shown in Fig.2. The section with continuously rising effective voltage up to the maximum level of 200 V at 50 Hz permits in the quasi-steady operational state almost a constant mechanical torque of 4.9 Nm, whereas the interval with constant maximal effective voltage magnitude is denoted as field weakening range, characterized with a constant mechanical power output of 770 W.

The desired high quality of the drive system is very sensitive to appearing higher harmonics in the electrical stator current or in the mechanical torque, even from unsuitable machine designs or inappropriate power converter strategies (Lipo et al., 1969; Stuart & Hebbar, 1971).

Such undesired current harmonics in converter driven motors can cause unforeseen losses and lead directly to additional heating effects inside the semiconductors and the winding system (Heimbrock & Seinsch, 2005). Mechanical problems regarding the rotating shaft can in particularly arise whenever frequencies in the generated mechanical torque spectrum coincide with natural resonance frequencies of the rotating shaft (Szabo, 1972).

The application of different commercial calculation tools within the design process of electrical drive systems gains crucial interest in order to overcome such problems. An extended finite element method with directly coupled electrical circuits for instance allows the treatment of the complete drive system in the time-domain. Thereby, the converter

topology is included by discrete electronic devices, whereas the induction motor is basically represented by iron laminations, insulation, stator winding and squirrel cage. The procedure overcomes previous insufficiencies and delivers results in dependency on well known control strategies with good accuracy.

2. Converter Topology and Control Unit

The power conversion from the public three-phase ac grid of constant frequency and voltage amplitude into an arbitrary three-phase ac system with variable settings is performed by means of the power converter topology in Fig.3.

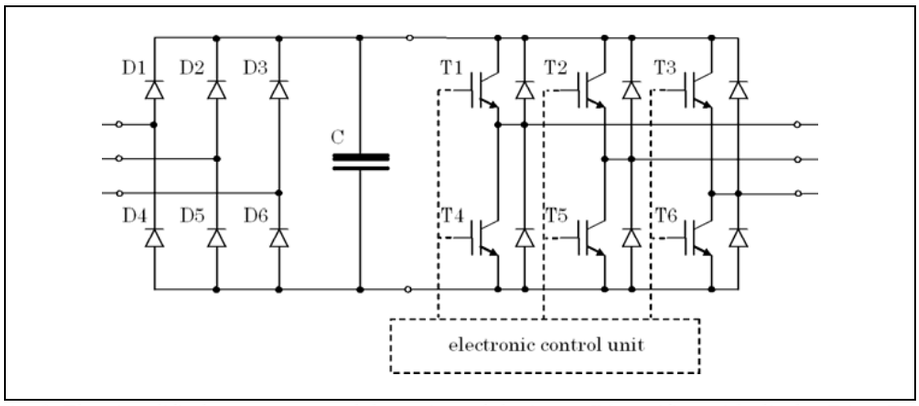

Fig. 3. The simplified converter model consists of the input B6 rectifier with diodes D1 to D6, the dc voltage link, three half-bridges formed by semiconductors T1-T4, T2-T5 and T3-T6 and an electronic control unit

The input ac to dc rectification is done by the diodes D1 to D6. The classical B6-bridge causes thereby an unavoidable voltage ripple. The capacitor smoothes these distinct fluctuations within the dc link level of 565 V, whereas the inductance restricts undesired current peaks during unexpected operational states (Kleinrath, 1980). The conversion of the dc link to three phase output ac power is exclusively performed in the switched mode.

The control unit in Fig.3 has the task to generate different duty cycles for the semiconductor devices T1 to T6. The most widely used method of pulse-width modulation employs carrier modulators in each of the three phases (Buja & Indri, 1977; Kliman & Plunkett, 1979; Murphy & Egan, 1983). A simple realization of the main control part is shown in Fig.4. The according time-dependent signal courses in the control unit are exemplarity depicted in Fig.5 for the maximum output voltage at the frequency of 50 Hz. The phase reference signal with the desired drive frequency 50 Hz is thereby sampled by a single saw-tooth carrier signals with a rate of 2 kHz. The electronic control unit generates signals for the semiconductors whenever the sine-wave and saw-tooth signal have the same value.

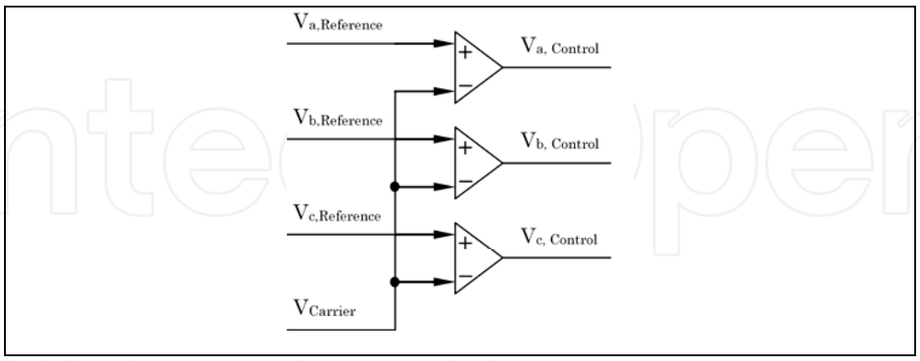

Fig. 4. Sampling of reference signals by a carrier signal

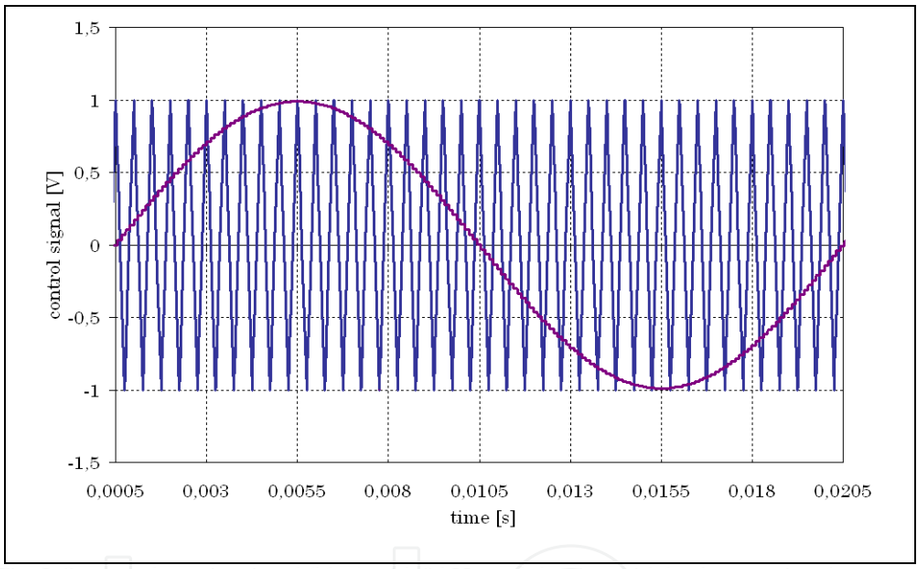

Fig. 5. Saw-tooth carrier signal (blue) with 2 kHz and the sinusoidal reference signal (magenta) with 50 Hz

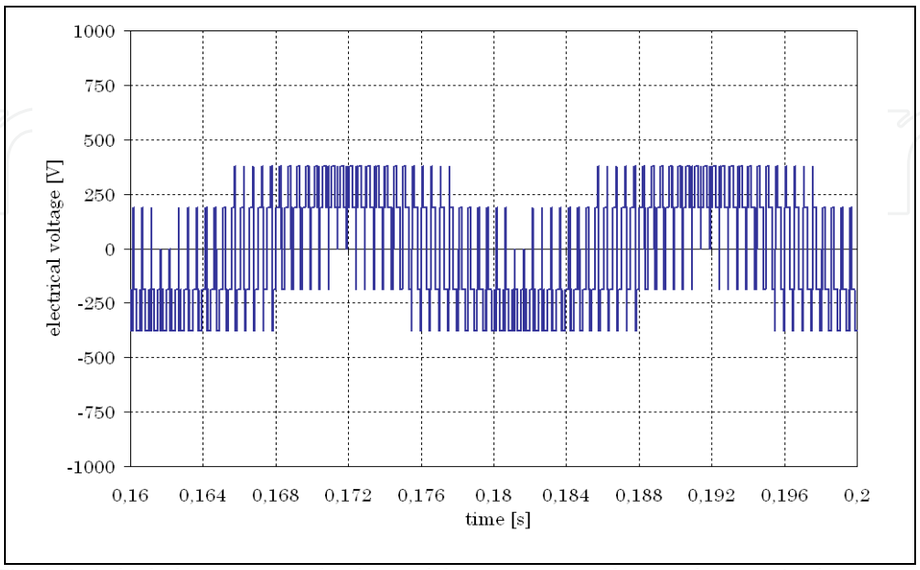

Fig. 6. Switched phase-to-neutral voltage of the star-connected motor for a carrier frequency of 2 kHz

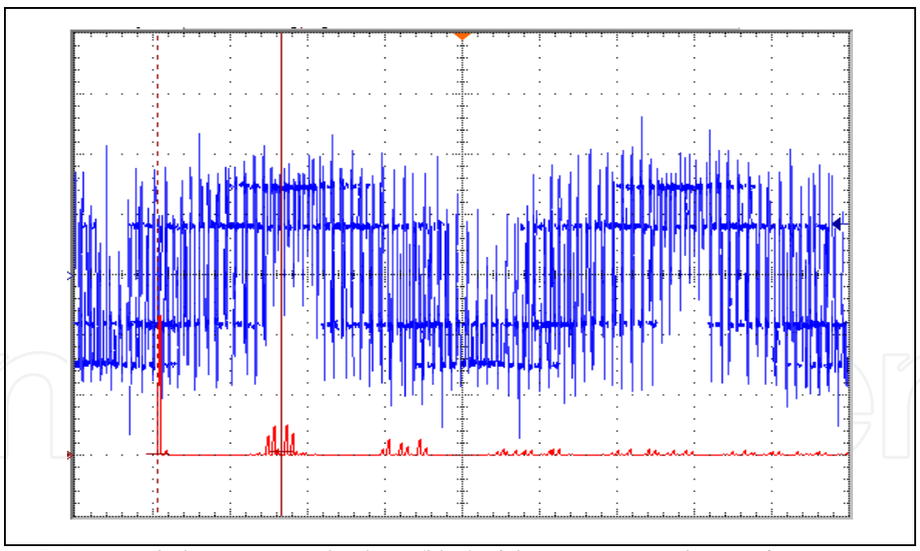

Fig. 7. Measured phase-to-neutral voltage (blue) of the star-connected motor for a carrier frequency of 2 kHz, whereby one division corresponds to 4 ms in the abscissa and 250 V in the ordinate. The Fourier spectrum (red) is based on 140 V per ordinate division

The utilized semiconductors effectuate temporary connections at high repetition rates with short rising times. The generated time-dependent phase-to-neutral output voltage in case of the used control method from Fig.4 shows within the numerical processed course in Fig.6 five distinct voltage levels. The fundamental content of the effective motor voltage is thereby 200 V at 50 Hz, as it was required for that specific steady operational state in Fig.2. The numerical calculation uses idealized switches within the power converter and neglects the motor feed cable in Fig.3.

The measured courses in Fig.7 look slightly different to that in Fig.6 because of the non-ideal effects of the motor feed cable and additionally appearing capacitive influences of the complete stator winding system. Some distinct voltage peaks are obvious in Fig.7 due to voltage reflection at the motor terminals without using additional filters.

3. Field-Circuit Coupling Technique

The local field quantities of the applied 2D finite element algorithm must be coupled to external circuits in order to include the source voltage waveforms of the converter (Silvester, 1995).

The finite element representation of the axially un-skewed stator lamination is exemplarily given in Fig.8. The modelling of the voltage-fed stator winding system in Fig.9 generally demands a distinct number of series connected bars in order to form one single coil. The stator phase resistor and the stator phase inductance in Fig.9 represent the not modelled 3D end-winding effects within the 2D finite element calculation (Salon, 1996). All three stator phases are further star-connected. The supplied voltage at the external terminals in Fig.9 can thereby be arbitrarily varying by time.

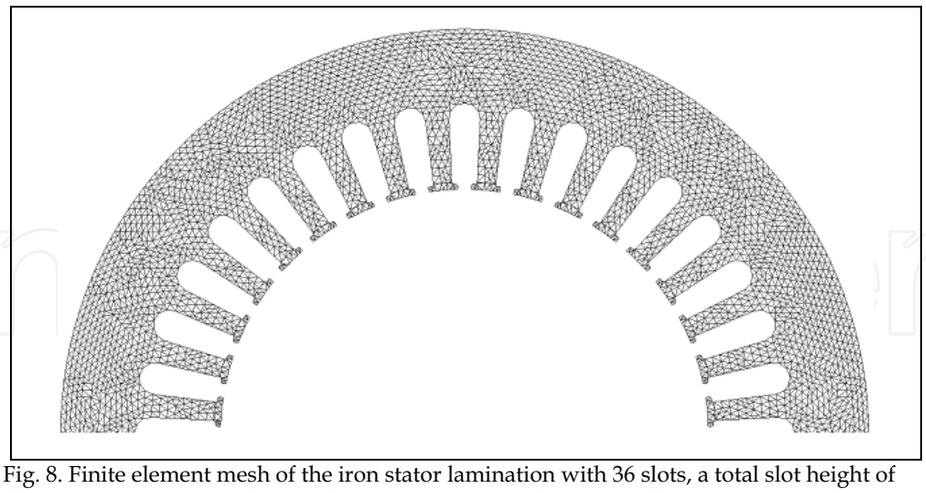

Fig. 8. Finite element mesh of the iron stator lamination with 36 slots, a total slot height of 13mm, an average slot width of 4mm, a stator yoke thickness of 11mm and a bore diameter of 75.5mm

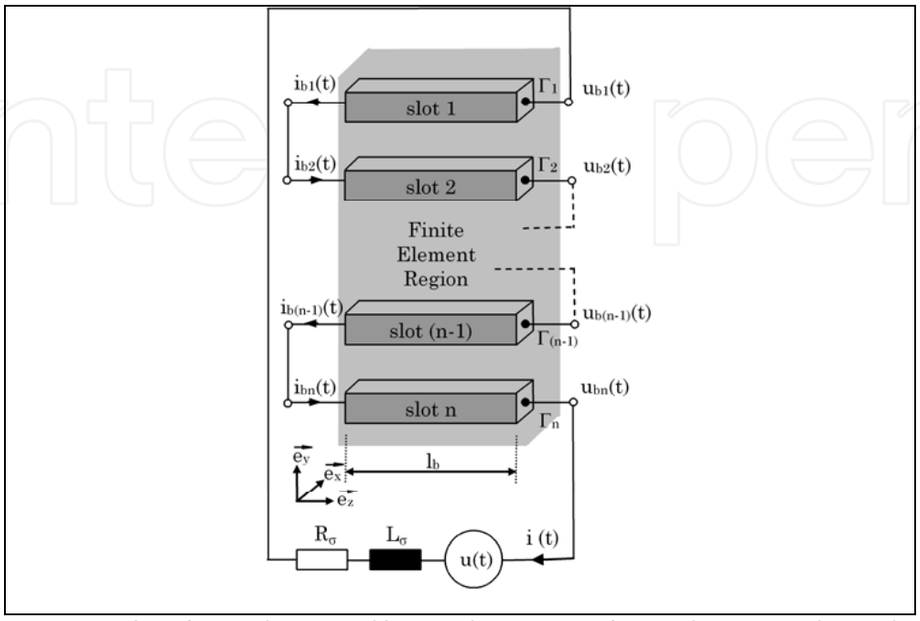

Fig. 9. A number of n-serial connected bars, each consisting of 90 single wires inside one slot, are forming one stator coil with 540 windings inside the plane finite element domain, whereas both external resistive and inductive parameters are representing 3D stator effects

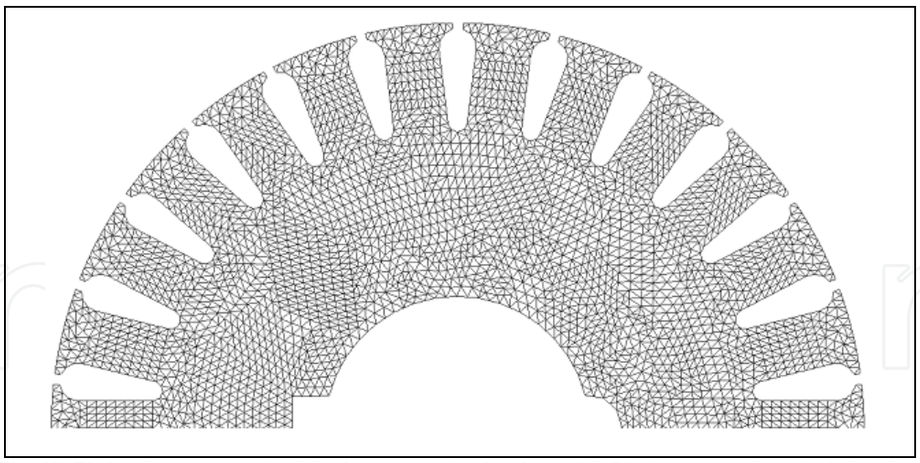

Fig. 10. Finite element mesh of the iron rotor lamination with 26 slots, a total slot height of 9.2mm, an average slot width of 2.6mm, a bore diameter of about 75mm, a rotor yoke thickness of 16mm and a shaft diameter of about 25mm

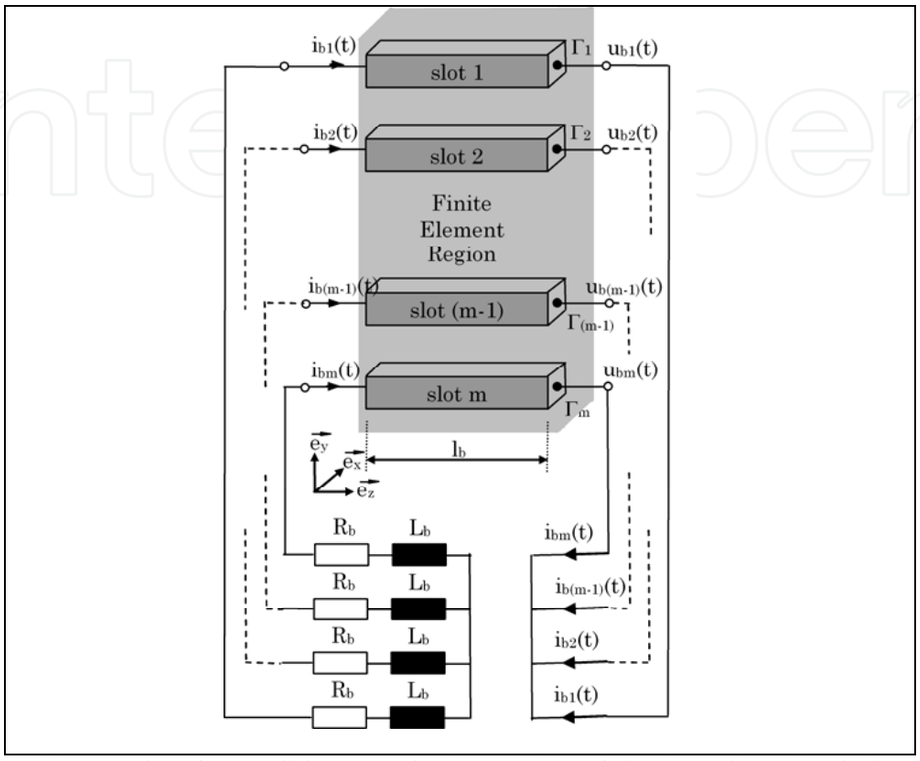

Fig. 11. A number of m-parallel connected coils, consisting of aluminum die casting, built up the squirrel cage rotor inside the plane finite element domain, whereas the external resistive and inductive parameters are implicit representing 3D end-ring effects

The exemplarity depicted time-dependent voltage waveform in Fig.6 is governed by very fast rising/falling voltage flanks, which have to be processed within the coupled numerical finite element analysis. Unfortunately, the chosen time-step for solving such problems is often smaller than 10 ns (Istfan, 1987; Biro et al., 1996).

The used 2D finite element model of the un-skewed rotor depicted in Fig.10 is not suitable to account for 3D end-ring effects. The complete winding schema for the not skewed squirrel cage rotor is shown in Fig.11, whereby the combined parameters approximately take account of 3D influences.

The finite element approach allows the computation of the acting magnetic force on the solid rotor by *virtual motion* as sum over local contributions (DeBortoli, 1992). The rotor moves on stepwise with the aid of the applied *band technique* (Davat et al., 1985). Thus, elements which are situated at these band domain may be deformed during motion since some of their nodes may follow the moving rotor reference frame and some the stationary

stator one (Palma, 1989). These element distortions are occurring in dependency on the movement. So, the continuous element distortion enforces a re-meshing of air-gap elements lying on the band.

Due to the non-linear iron material properties, as listed in Table 1, linearization and time-discretization methods are necessary to solve such coupled electromechanical problems in the time domain (Bins et al., 1992; Bathe, 1996; Schwarz, 1984).

B [T]	0	0.4	0.8	1.2	1.6	2.0
H [A/m]	0	140	190	260	1370	20500

Table 1. Non–linear iron magnetization characteristic

4. Electric Input Current and the Mechanical Output Torque

The analysis of the time-dependent courses of the electrical current and the mechanical torque within inverter driven motors in the time-domain is of main importance, because it allows further estimations about additionally heating effects as well as critically resonance frequencies of the rotating shaft.

4.1 Time dependent electrical current courses and their harmonic spectrum

The numerical analysis of the complete voltage-fed drive system with respect to the course depicted in Fig.6 for a carrier frequency of 2 kHz delivers the time-dependent electrical stator current as depicted in Fig.12. The application of the series-expansion

$$\mathrm{i}(\mathrm{t}) = \sum_{\mathrm{k}=1}^{\infty} \hat{\mathrm{I}}_{\mathrm{k}} \sin\left(2\pi \mathrm{kf} \cdot \mathrm{t} + \alpha_{\mathrm{k}}\right) \tag{1}$$

delivers several harmonic components. Thereby, the distinct fundamental component at the frequency of 50 Hz, and additionally the undesired first side pair harmonics at 1950 Hz and 2050 Hz as well as the second side pair harmonics at 3950 Hz and 4050 Hz can be found in the complete spectrum of Fig.13. Higher harmonic contributions show relatively small magnitudes and are therefore only of secondary interest.

The measured electrical current course and the according harmonic analysis are depicted in Fig.14. Not only the comparison of the time-courses with those in Fig.12, even though the harmonic magnitudes received from (1) show a good conformity.

In spite of some differences between the numerical processed voltage shape in Fig.6 and the measured voltage in Fig.7, in particular during the switching on/off state, no significant discrepancy between the numerical calculated and the measured time-dependent current distribution in Fig.12 and Fig.14, respectively, can be found due to the distinct inductive behaviour of the squirrel cage induction motor.

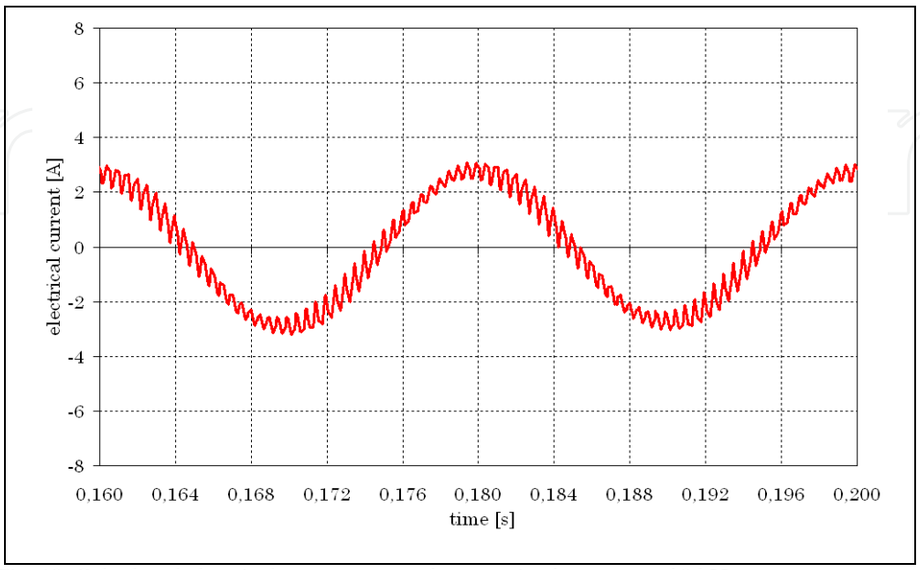

Fig. 12. Calculated electrical motor current for a carrier frequency of 2 kHz

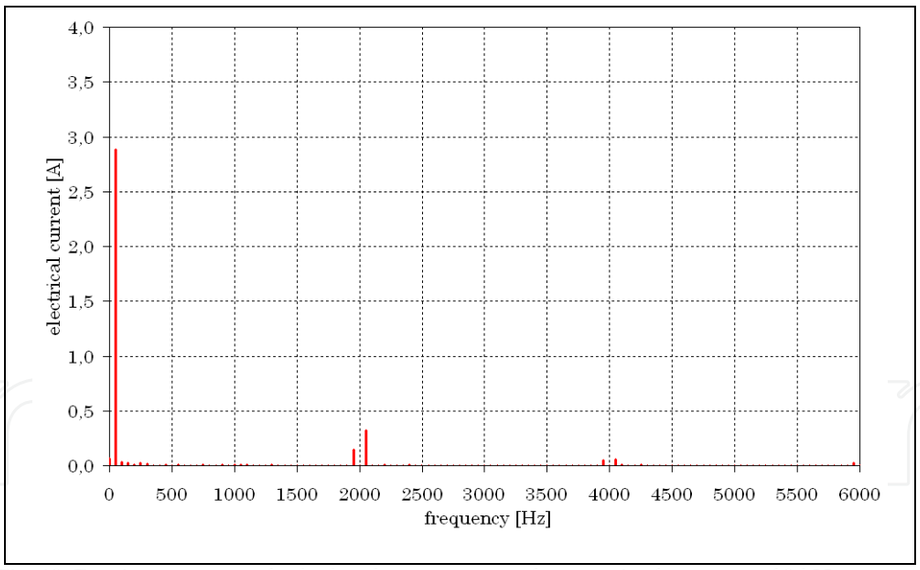

Fig. 13. Fourier spectrum of calculated motor current for a carrier frequency of 2 kHz

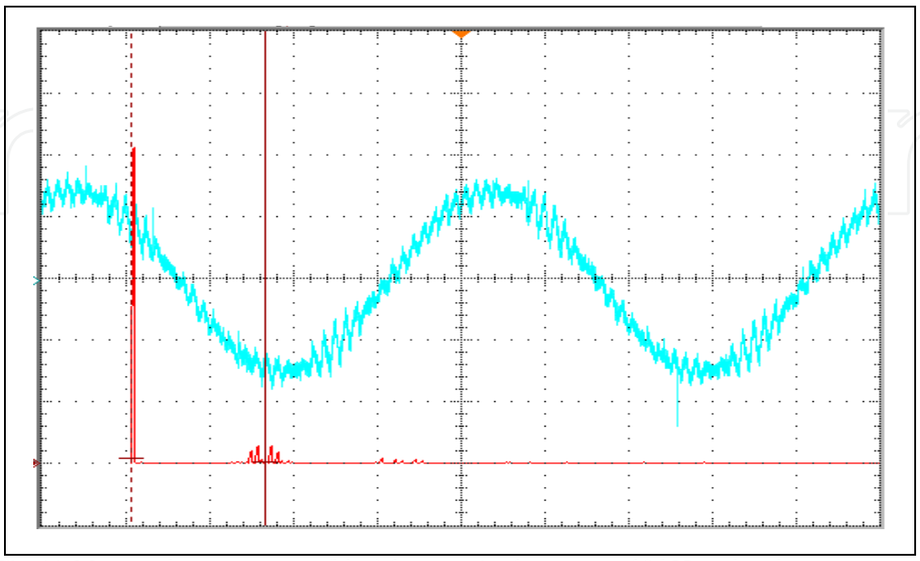

Fig. 14. Measured motor current (blue) for a carrier frequency of 2 kHz, whereby one division corresponds to 4 ms in the abscissa and 2 A in the ordinate. The Fourier spectrum (red) is based on 0.6 A per ordinate division

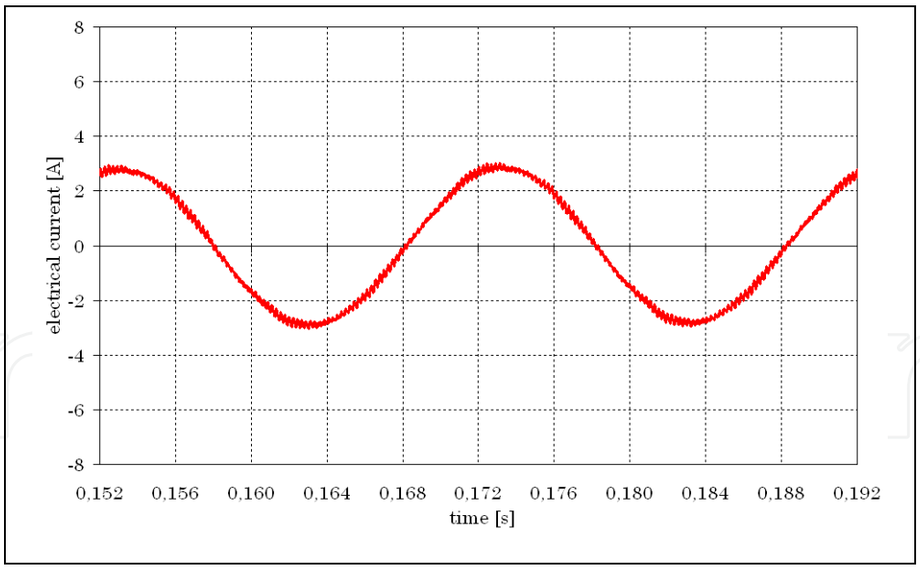

Fig. 15. Calculated electrical motor current for a carrier frequency of 4.5 kHz

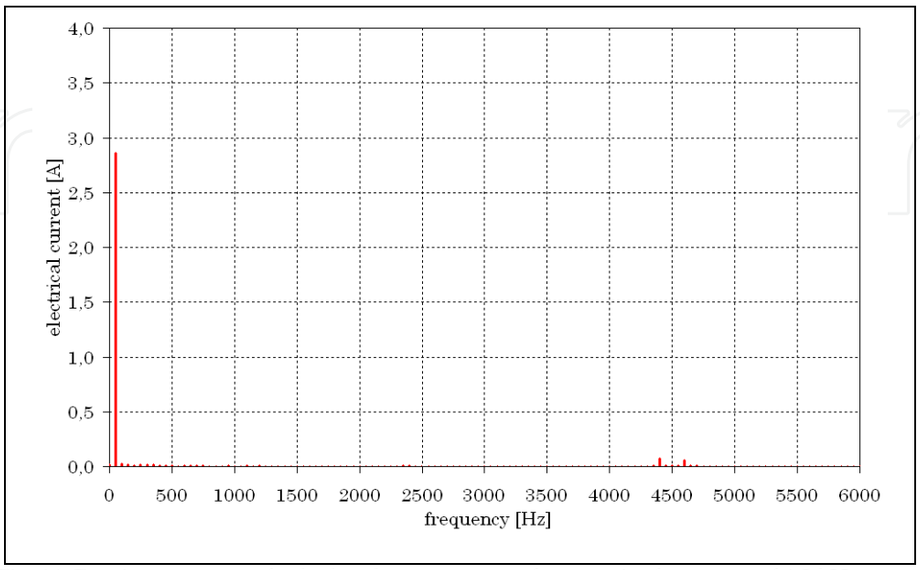

Fig. 16. Fourier spectrum of calculated motor current for a carrier frequency of 4.5 kHz

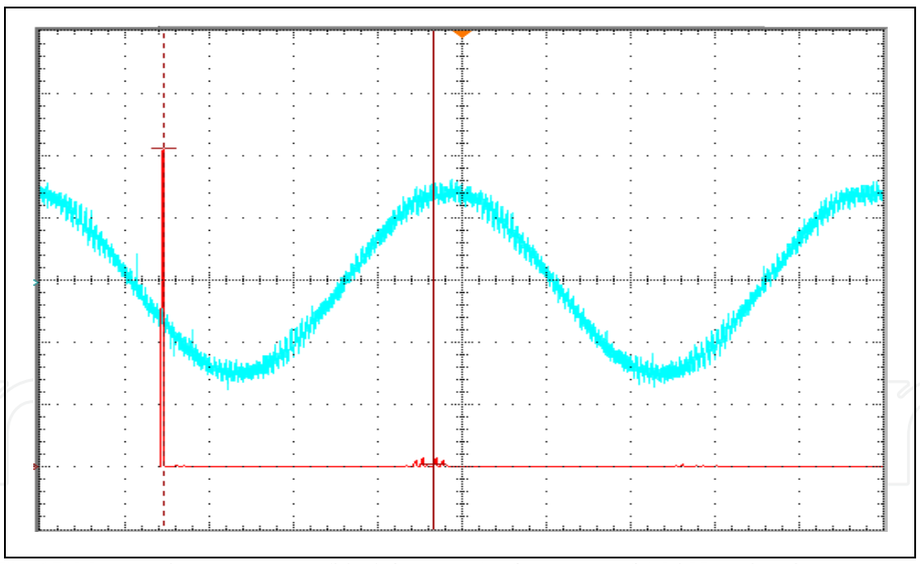

Fig. 17. Measured motor current (blue) for a carrier frequency of 4.5 kHz, whereby one division corresponds to 4 ms in the abscissa and 2 A in the ordinate. The Fourier spectrum (red) is based on 0.6 A per ordinate division

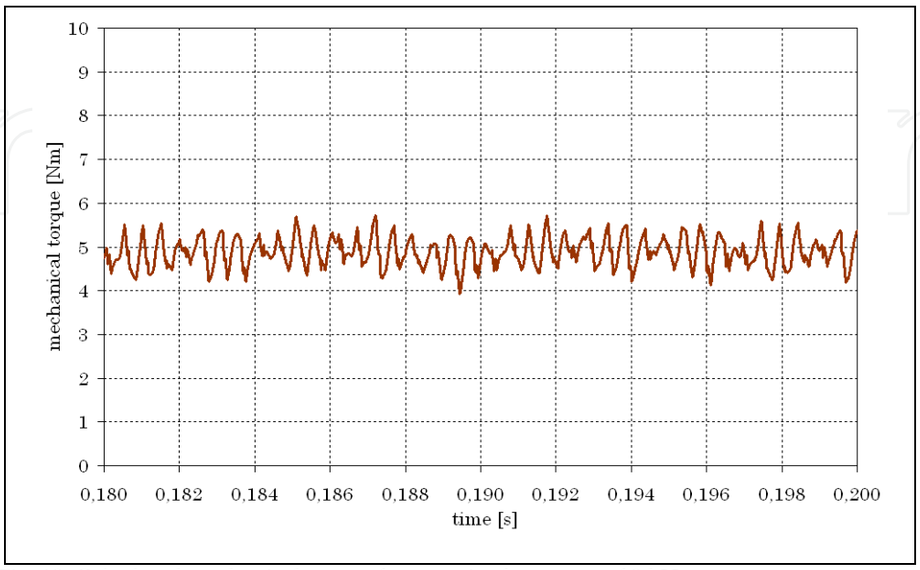

Fig. 18. Calculated mechanical torque for a carrier frequency of 2 kHz

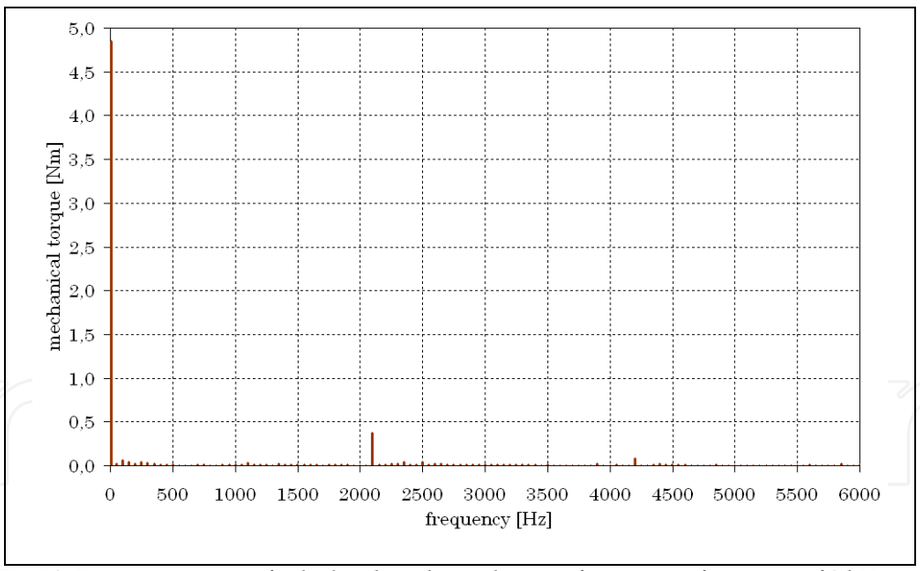

Fig. 19. Fourier spectrum of calculated mechanical torque for a carrier frequency of 2 kHz

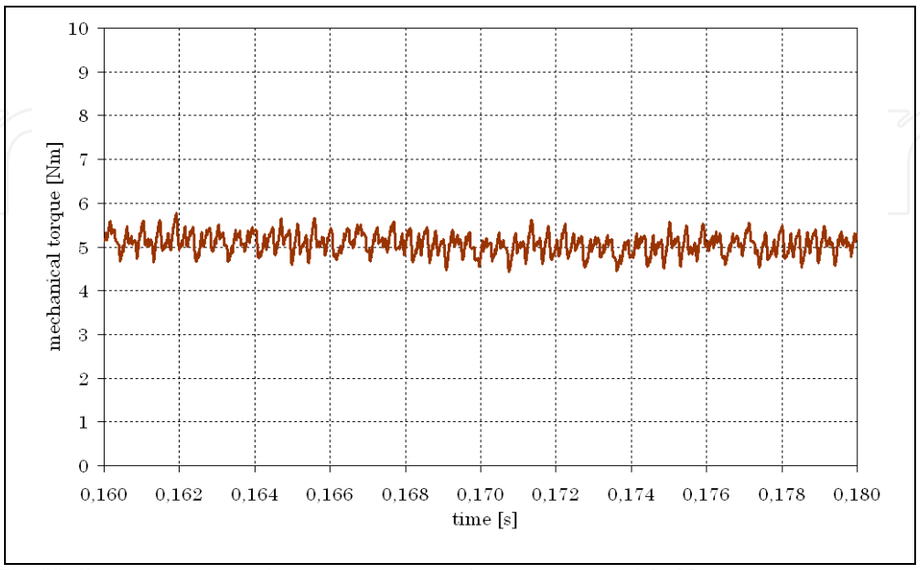

Fig. 20. Calculated mechanical torque for a carrier frequency of 4.5 kHz

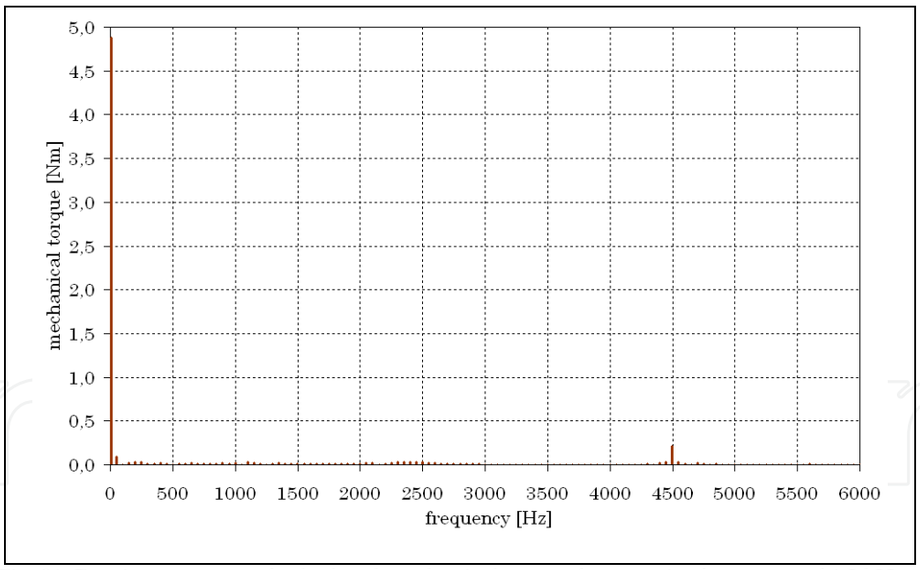

Fig. 21. Fourier spectrum of calculated mechanical torque for a carrier frequency of 4.5 kHz

In order to smooth the overlaid current ripple within the distribution in Fig.12, the first harmonic pair in Fig.13 caused by the carrier frequency of 2 kHz has to be eliminated by increasing the frequency to 4.5 kHz.

The improvement within the electrical current quality is shown in Fig.15. The course is very similar to the desired sinusoidal one. That circumstances are also obvious from the associated spectrum (1) depicted in Fig.16. Beside the desired fundamental component, only a first sideband frequency at 4400 Hz and 4600 Hz exists. From a comparison of the numerical calculated results from Fig.15 and Fig.16 with the measured quantities in Fig.17 it is obvious, that a good agreement could be achieved by the proposed numerical modelling and calculation method.

4.2 Time dependent mechanical torque courses and their harmonic spectrum

The numerical calculated time-dependent mechanical torque is depicted in Fig.18 for a control strategy based on the carrier frequency of 2 kHz. The series-expansion

$$\mathrm{m}(\mathrm{t}) = \sum_{\mathrm{k}=0}^{\infty} \hat{\mathrm{M}}_{\mathrm{k}} \sin\left(2\pi \mathrm{kf} \cdot \mathrm{t} + \beta_{\mathrm{k}}\right) \tag{2}$$

leads to the harmonic torque magnitudes, which are further shown in Fig.19. Beside the desired constant contribution, a very distinct undesired torque fluctuation due to the converter topology of Fig.3 is caused at the frequency of 2100 Hz. Other contributions to the torque ripple are obviously suppressed.

A significant improved spectrum could be achieved by increasing the carrier frequency up to 4.5 kHz. The analysis of the numerical results from Fig.20 in the frequency domain delivers the torque spectrum shown in Fig.21. The previously torque components are shifted to the higher ordinal frequency of 4500 Hz, but the relevant magnitudes are significantly reduced. A comparison of Fig.18 with Fig.20 shows that effect imposingly.

Thus, undesired effects concerning the quality of the true shaft motion of the drive system could be avoided by using higher carrier frequencies within the used power converter.

5. Conclusion

The prediction of undesired current and torque harmonics inside converter-fed induction motors is of crucial interest in order to guarantee a high quality level of the drive system. Thereby, the complex interaction of the converter and the squirrel cage induction motor has to be considered. This is done by using the 2D transient electromagnetic-mechanical finite element method with additionally coupled external circuits. Fortunately, the generated arbitrary time-dependent output voltage waveforms of the converter are directly processed within the non-linear finite element analysis in the time-domain. Effects of minor changes in the mechanical rotor true running due to the torque ripple as well as fluctuations in the electrical current consumption are considered. This kind of *virtual design* delivers a very systematically and deep insight into the interaction of several involved drive components, such as e.g. power converter topology, squirrel cage induction machine and control strategy,

within the overall design. Consequently, the method encourages a straightforward and reliable industrial development process of complex electrical drive systems.

6. References

Bathe K.J. (1996). *Finite Element Procedures,* Prentice Hall, New Jersey

Bins K.J., Lawrenson P.J. & Trowbridge C.W. (1992). *The Analytical and Numerical Solution of Electric and Magnetic Fields,* John Wiley & Sons, Chichester

Biro O., Preis K. & Richter K.R. (1996). On the Use of the Magnetic Vector Potential in the Nodal and Edge Finite Element Analysis of 3D Magnetostatic Problems. *IEEE Transactions on Magnetics,* Vol. 32, No. 5.

Buja G.S. & Indri G.B. (1977). Optimal Pulse Width Modulation for Feeding AC Motors. *IEEE Transactions on Industry Applications,* Vol. IA-13, No. 1.

Davat B., Ren Z. & Lajoic-Mazenc M. (1985). The movement in field modeling. *IEEE Transactions on Magnetics,* Vol. 21, No. 6.

DeBortoli M.J. (1992). Extensions to the Finite Element Method for the Electromechanical Analysis of Electrical Machines, *Rensselaer Polytechnic Institute New York,* PhD Thesis.

Heimbrock A. & Seinsch H.O. (2005). Neue Erkenntnisse über Oberschwingungsverluste in Umrichtergespeisten Käfigläufern. *Elektrotechnik und Informationstechnik,* Vol. 122, No. 7.

Heintze K., Tappeiner H. & Weibelzahl M. (1971). Pulswechselrichter zur Drehzahl-steuerung von Asynchronmaschinen. *Siemens Zeitschrift,* Vol.3, No.45.

Istfan B. (1987). Extensions to the Finite Element Method for Nonlinear Magnetic Field Problems, *Rensselaer Polytechnic Institute New York,* PhD Thesis.

Kleinrath H. (1980). *Stromrichtergespeiste Drehfeldmaschinen,* Springer Verlag, Wien

Kliman G.B. & Plunkett A.B. (1979). Development of a Modulation Strategy for a PWM Inverter Drive. *IEEE Transactions on Industry Applications,* Vol. IA-15, No. 1.

Lipo T.A., Krause P.C. & Jordan H.E. (1969). Harmonic Torque and Speed Pulsation in a Rectifier-Inverter Induction Motor Drive. *IEEE Transactions on Power Apparatus and Systems,* Vol. PAS-88, No. 5.

Murphy J.M.D. & Egan M.G. (1983). A Comparison of PWM Strategies for Inverter-Fed Induction Motors. *IEEE Transactions on Industry Applications,* Vol. IA-19, No. 3.

Palma R. (1989). Transient Analysis of Induction Machines using Finite Elements, *Rensselaer Polytechnic Institute New York,* PhD Thesis.

Salon J.S. (1996). *Finite Element Analysis of Electrical Machines,* Cambridge University Press, Cambridge

Schwarz R. (1984). *Methode der Finiten Elemente,* Teubner, Stuttgart

Silvester P.P. (1995). *Finite Elements for Electrical Engineers,* Kluwer Academic Publisher, Boston/London

Stuart D.T. & Hebbar K.M. (1971). Torque Pulsation in Induction Motors with Inverter Drives. *IEEE Transactions on Industry and General Applications,* Vol. GA-7, No. 2.

Szabo I. (1972). *Technische Mechanik,* Springer Verlag, Berlin

Advances in Computer Science and IT

Edited by D M Akbar Hussain

ISBN 978-953-7619-51-0
Hard cover, 420 pages
Publisher InTech
Published online 01, December, 2009
Published in print edition December, 2009

The book presents some very interesting and excellent articles for this divergent title. The 22 chapters presented here cover core topics of computer science such as visualization of large databases, security, ontology, user interface, graphs, object oriented software developments, and on the engineering side filtering, motion dynamics, adaptive fuzzy logic, and hyper static mechanical systems. It also covers topics which are combination of computer science and engineering such as meta computing, future mobiles, colour image analysis, relative representation and recognition, and neural networks. The book will serve a unique purpose through these multi-disciplined topics to share different but interesting views on each of these topics.

InTech Europe
University Campus STeP Ri
Slavka Krautzeka 83/A
51000 Rijeka, Croatia
Phone: +385 (51) 770 447
Fax: +385 (51) 686 166
www.intechopen.com

InTech China
Unit 405, Office Block, Hotel Equatorial Shanghai
No.65, Yan An Road (West), Shanghai, 200040, China
中国上海市延安西路65号上海国际贵都大饭店办公楼405单元
Phone: +86-21-62489820
Fax: +86-21-62489821

IntechOpen